Nanoscale

COMMUNICATION

View Article Online
View Journal | View Issue

Cite this: *Nanoscale*, 2022, **14**, 14023

Received 30th April 2022,
Accepted 9th June 2022

DOI: 10.1039/d2nr02364d

rsc.li/nanoscale

Ultrathin Ti-doped WO_3 nanosheets realizing selective photoreduction of CO_2 to CH_3OH†

Peiquan Ling,‡[a] Juncheng Zhu,‡[a] Zhiqiang Wang,[a] Jun Hu,[a] Junfa Zhu,[a] Wensheng Yan,[a] Yongfu Sun*[a,b] and Yi Xie*[a,b]

Arduous CO_2 activation and sluggish charge transfer retard the photoreduction of CO_2 to CH_3OH with high efficiency and selectivity. Here, we fabricate ultrathin Ti-doped WO_3 nanosheets possessing approving active sites and optimized carrier dynamics as a promising catalyst. Quasi *in situ* X-ray photoelectron spectroscopy and synchrotron–radiation X-ray absorption near-edge spectroscopy firmly confirm that the true active sites for CO_2 reduction are the W sites rather the Ti sites, while the Ti dopants can facilitate charge transfer, which accelerates the generation of crucial COOH* intermediates as revealed by *in situ* Fourier-transform infrared spectroscopy and density functional theory calculations. Besides, the Gibbs free energy calculations also validate that Ti doping can lower the energy barrier of CO_2 activation and CH_3OH desorption by 0.22 eV and 0.42 eV, respectively, thus promoting the formation of CH_3OH. In consequence, the Ti-doped WO_3 ultrathin nanosheets show a superior CH_3OH selectivity of 88.9% and reach a CH_3OH evolution rate of 16.8 μmol g^{-1} h^{-1}, about 3.3 times higher than that on WO_3 nanosheets. This work sheds light on promoting CO_2 photoreduction to CH_3OH by rational elemental doping.

Artificial photosynthesis, which involves the conversion of carbon dioxide (CO_2) into value-added fuels by solar energy, provides a sustainable way to solve the disturbing energy crisis and climate change.[1–4] Various carbon-containing products can be acquired through the CO_2 photoreduction reaction, among which methanol (CH_3OH) is one of the liquid products with the most potential due to its extensive applications.[5–7] For instance, CH_3OH can be directly used in fuel cells[8] and is the precursor of numerous fundamental chemicals like aromatics, C_2H_4, methyl methacrylate and fatty acid methyl esters.[5,9] It is reported that the global demand for CH_3OH can reach more than 100 million tons per year.[10] Unfortunately, the product selectivity towards CH_3OH in the conversion of CO_2 with H_2O is still insufficient and unsatisfactory. Obstacles arise from the arduous activation of inert CO_2 molecules (C═O dissociation energy of ~750 kJ·mol^{-1}).[11,12] Most importantly, the 6-electron transfer process during CH_3OH formation causes strict kinetic limitation, making it harder to generate CH_3OH than other products (*e.g.* CO).[13–15] In addition, many existing photocatalysts suffer from a narrow light adsorption range and the poor separation efficiency of photogenerated carriers, which hinder the charge transfer from the catalysts to the adsorbed CO_2.[16–20] Hence, designing catalysts with outstanding carrier dynamics and approving active sites is essential for realizing highly efficient CO_2 photoreduction into CH_3OH.

To meet the above requirements, constructing ultrathin two-dimensional (2D) nanosheets with appropriate elemental doping is a very promising solution. On the one hand, ultrathin 2D nanosheets can provide abundant active sites for CO_2 adsorption and activation due to their high specific surface area and sufficient uncoordinated atoms.[21–23] Their light absorption ability is also different from that of the traditional bulk catalysts, while the efficiencies of photogenerated carrier separation and charge transfer can be promoted thanks to their reduced migration paths.[24–28] On the other hand, elemental doping can regulate the electron structure of active atoms, further expediting CO_2 activation and reduction.[29,30] It can also change the band structure of catalysts and extend their light absorption range, making the catalysts more suitable for CO_2 photoreduction.[31–33] Furthermore, suitable elemental doping can optimize the photogenerated carrier dynamics, alter the reaction energy barrier and control reaction intermediates, enhancing product selectivity towards the desired species.[29,30,34] Therefore, it is prospective to boost CO_2 photoreduction to CH_3OH through synthesizing ultrathin 2D

[a]*Hefei National Research Center for Physical Sciences at the Microscale, National Synchrotron Radiation Laboratory, University of Science and Technology of China, Hefei 230026, China. E-mail: yfsun@ustc.edu.cn, yxie@ustc.edu.cn*
[b]*Institute of Energy, Hefei Comprehensive National Science Center, Hefei 230031, China*

†Electronic supplementary information (ESI) available. See DOI: https://doi.org/10.1039/d2nr02364d

‡These authors contributed equally to this work.

nanosheets with elemental doping. In this regard, inexpensive and eco-friendly tungsten oxide (WO_3) is one of the promising candidates, thanks to its suitable band gap, good light-harvesting ability and easily tunable electron structure.[35,36] Although WO_3 nanosheets have been applied in many photochemical fields,[36–38] their performance in CO_2 photoreduction to CH_3OH still lacks exploration.

In this work, Ti-doped WO_3 ultrathin nanosheets were fabricated *via* an acid-assisted method. X-ray photoelectron spectroscopy (XPS), synchrotron–radiation X-ray absorption near-edge spectroscopy (XANES) and element mappings show the successful doping of Ti into WO_3 nanosheets, while photoluminescence (PL) and time-resolved photoluminescence spectra (TRPL) reveal the enhanced separation of photogenerated carriers due to the Ti doping. Besides, quasi *in situ* XPS spectra and quasi *in situ* XANES spectra firmly validate that the true active sites are the W sites rather the Ti sites, where the Ti dopants facilitate the charge transfer, which is beneficial for the formation of COOH* species, one of the most important intermediates for carbon products during CO_2 reduction. *In situ* Fourier-transform infrared (FTIR) spectroscopy demonstrates this conclusion by the stronger intensity of COOH* species on Ti-doped WO_3 nanosheets. In addition, density functional theory (DFT) calculations confirm that Ti doping can strengthen the bonding between COOH* intermediates and catalysts, while the energy barrier of CO_2 activation and CH_3OH desorption is decreased by 0.22 eV and 0.42 eV, respectively, which dramatically facilitates the formation of CH_3OH. As a result, the Ti-doped WO_3 ultrathin nanosheets show a superior CH_3OH selectivity of 88.9% and achieve a CH_3OH evolution rate of 16.8 μmol g^{-1} h^{-1}, about 3.3 times higher than that on the WO_3 nanosheets. This work offers an effective approach to enhance the conversion of CO_2 and H_2O into CH_3OH through elemental doping.

To obtain a non-toxic and efficient catalyst for CO_2 photoreduction, the ultrathin Ti-doped WO_3 nanosheets (called Ti–WO_3 nanosheets for short) were fabricated *via* an acid-assisted method. The powder X-ray diffraction (XRD) patterns of the Ti–WO_3 nanosheets could be indexed well to JCPDS no. 89-1287 and no additional peak was detected, indicating the successful synthesis of pure tetragonal WO_3 (Fig. 1A). The transmission electron microscopy (TEM) image showed that Ti-doped WO_3 had a sheet-like morphology (Fig. 1B). Meanwhile, the high-resolution TEM (HRTEM) image showed two interplanar spacings of 0.367 nm and 0.382 nm with a dihedral angle of 90°, corresponding to the (200) and (001) planes of tetragonal WO_3, which demonstrated their [010] orientation (Fig. 1C). The atomic force microscopy (AFM) image demonstrated that the thickness of the Ti–WO_3 nanosheets was about 2.20 nm (Fig. 1D), which was approximately the thickness of the triple-unit-cell slab along the [010] direction, illustrating the successful fabrication of ultrathin Ti–WO_3 nanosheets. For comparison, the undoped WO_3 nanosheets (called WO_3 nanosheets for short) were obtained without the addition of Ti sources during the synthesis. The WO_3 nanosheets had the same crystalline phase, growth orientation and thickness as the Ti–WO_3 nanosheets (Fig. S1†). It is worth mentioning that

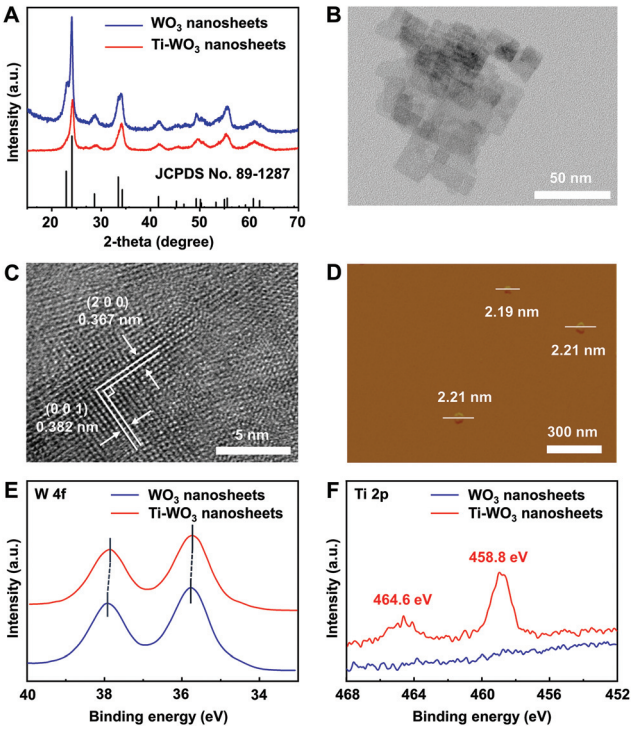

Fig. 1 (A) XRD patterns of the Ti–WO_3 nanosheets and the WO_3 nanosheets. (B) TEM image of the Ti–WO_3 nanosheets. (C) HRTEM image of the Ti–WO_3 nanosheets, showing the 0.367 nm and 0.382 nm interplanar distances that matched well with the d_{200} and d_{001} planes, respectively. (D) AFM image of the Ti–WO_3 nanosheets. (E) XPS spectra of W 4f and (F) Ti 2p for the Ti–WO_3 nanosheets and the WO_3 nanosheets.

the crystallinity of the Ti–WO_3 nanosheets was lower than that of the WO_3 nanosheets (Fig. 1A), which could be ascribed to the successful Ti doping into WO_3.[39,40] In addition, the Ti doping also slightly decreased the interplanar spacings in the Ti–WO_3 nanosheets (Fig. 1C and S1†), which was in agreement with a previous study.[40]

To further confirm that the Ti dopants had been doped in WO_3 nanosheets, X-ray photoelectron spectroscopy (XPS) of W 4f and Ti 2p was performed. As shown in Fig. 1E, there were two peaks at around 37.90 eV and 35.75 eV, corresponding to W $4f_{5/2}$ and W $4f_{7/2}$ states, respectively. Notably, both W $4f_{5/2}$ and W $4f_{7/2}$ in the Ti–WO_3 nanosheets exhibited a slightly negative shift, implying that some electrons were transferred to W^{6+} after Ti doping, resulting in more W^{5+} species.[35] This phenomenon was due to the partial replacement of W^{6+} by the Ti atoms.[41] In addition, there was no Ti 2p signal detected in the WO_3 nanosheets, while Ti 2p in the Ti–WO_3 nanosheets showed two peaks at 458.7 eV and 464.4 eV, which could be ascribed to the Ti(IV) $2p_{3/2}$ peak and the Ti(IV) $2p_{1/2}$ peak (Fig. 1F). This result was in accordance with the conclusion drawn from synchrotron–radiation X-ray absorption near-edge spectroscopy (XANES), which showed that the valence state of Ti in the Ti–WO_3 nanosheets was +4 (Fig. S2†). The content of Ti in the Ti–WO_3 nanosheets determined using inductively

coupled plasma atomic emission spectroscopy (ICP-OES) was 0.87 wt%, which was close to that determined by the XPS results (0.90 wt%). Furthermore, the annular dark-field TEM image and the corresponding element mappings revealed that there was no TiO_2 particle observed and the W, O and Ti elements were distributed uniformly (Fig. S3†). The Raman spectra also demonstrated that there was no additional peak detected in the Ti–WO_3 nanosheets (Fig. S4†), excluding the possibility of TiO_2/WO_3 heterojunction formation. Thus, these results showed that the Ti dopants had been doped in the WO_3 nanosheets and the valence state of Ti in the Ti–WO_3 nanosheets was +4.

To investigate the effect of Ti dopants on the electronic band structures, ultraviolet–visible (UV–vis) absorption spectra were recorded. As shown in Fig. 2A, the absorption spectrum of the Ti–WO_3 nanosheets showed a red-shift compared with that of the WO_3 nanosheets, implying the stronger visible light absorption on the Ti–WO_3 nanosheets.[21,31,35] In addition, the bandgap of the Ti–WO_3 nanosheets determined using the absorption spectra was 2.59 eV (Fig. 2B), which was smaller than that of the WO_3 nanosheets (2.66 eV). To obtain the band edge potentials of the samples, synchrotron–radiation photoemission spectroscopy (SRPES) was applied to measure the work functions and the valence band maxima (VBM).[36] As shown in Fig. 2C and D, the work functions of the Ti–WO_3 nanosheets and the WO_3 nanosheets could be calculated to be 4.30 and 4.53 eV, whereas their valence-band edges were located at 2.27 eV and 2.48 eV. Combined with the bandgaps obtained above, the electronic band structures of the Ti–WO_3 nanosheets and the WO_3 nanosheets could be estimated (Table S1†). It was obvious that both samples had suitable electronic band structures for reducing CO_2 to CH_3OH, confirming their potential applications in CO_2 photoreduction.[5]

To evaluate the effect of Ti dopants on the catalytic activity, photocatalytic CO_2 reduction experiments were carried out. The liquid products were analyzed using nuclear magnetic resonance (NMR) spectroscopy, while the gas products were analyzed using a gas chromatograph (GC) equipped with a thermal conductivity detector (TCD) and a flame ionization detector (FID). As displayed in Fig. 3A, CH_3OH was the major product of CO_2 photoreduction on both the samples, since the CO evolution rate was much lower than the CH_3OH evolution rate. The CH_3OH evolution rate on the Ti–WO_3 nanosheets could reach 16.8 μmol g^{-1} h^{-1}, which was about 3.3 times higher than that on the WO_3 nanosheets, suggesting that Ti doping could efficiently promote the catalytic activity of WO_3 nanosheets. The selectivity towards CH_3OH also increased from 80.0% to 88.9%. In addition, the CH_3OH evolution rate was related to the amount of Ti dopants (Fig. S5†), indicating that Ti doping was a feasible strategy to adjust the performance of WO_3 nanosheets during the CO_2 photoreduction. What's more, the control experiments demonstrated that CO_2, the Ti–WO_3 nanosheets (catalyst) and illumination were prerequisites for the CH_3OH formation, indicating that CH_3OH was derived from photocatalytic CO_2 reduction over the Ti–WO_3 nanosheets (Fig. 3B). This conclusion could be further verified by the $^{13}CO_2$ labelling experiments performed with synchrotron-based vacuum ultraviolet photoionization mass spectrometry (SVUV-PIM). As shown in Fig. S6,† N_2, CO and CO_2 could not be ionized when the photon energy was set at 11.50 eV, and thus one could eliminate the interference from their fragments.[42] Hence, the Ti–WO_3 nanosheets produced the product $^{13}CH_3OH$ (m/z = 33), confirming that evolved CH_3OH indeed originated from the photoreduction of CO_2 (Fig. 3C). Furthermore, the CH_3OH evolution rate showed almost no decay after 4 cycles of the photoreduction test (Fig. 3D), indicating the good photocatalytic stability of the

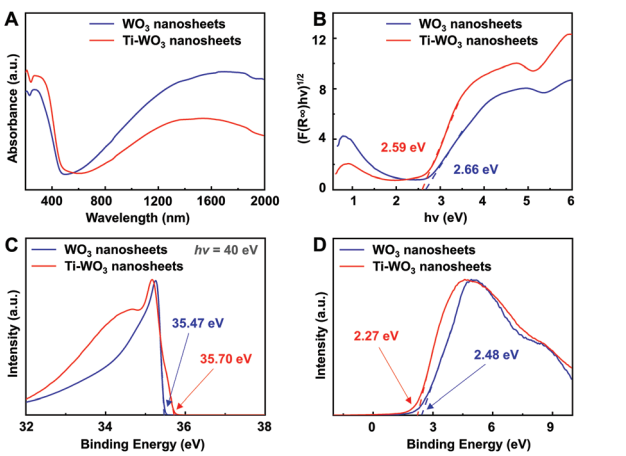

Fig. 2 (A) UV–vis absorption spectra and (B) the corresponding optical bandgaps for the Ti–WO_3 nanosheets and the WO_3 nanosheets. (C) Secondary electron cutoff and (D) valence band spectra of the Ti–WO_3 nanosheets and the WO_3 nanosheets acquired by synchrotron–radiation photoemission spectra.

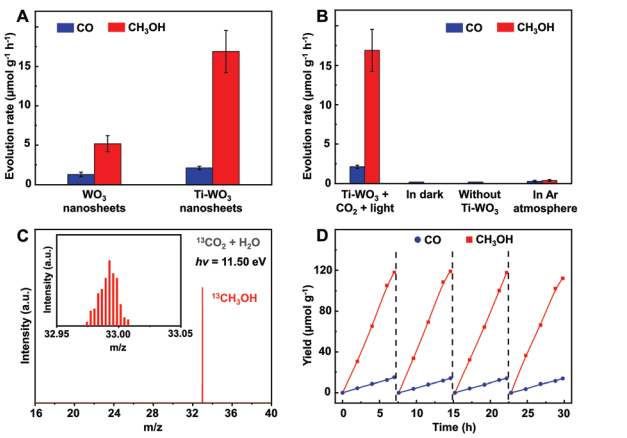

Fig. 3 (A) Products of the photocatalytic CO_2 reduction over the Ti–WO_3 nanosheets and the WO_3 nanosheets. The error bars represent the standard deviations of three independent measurements. (B) Products of photocatalytic CO_2 reduction over the Ti–WO_3 nanosheets under different conditions. (C) SVUV-PIMS spectrum of the products during $^{13}CO_2$ labeled photoreduction over the Ti–WO_3 nanosheets at $h\nu$ = 11.50 eV. Inset: signals of m/z = 33 ($^{13}CH_3OH$). (D) Cycling measurements for CO_2 photoreduction over the Ti–WO_3 nanosheets.

Ti–WO_3 nanosheets. The corresponding XRD patterns and TEM images after catalysis could also affirm the good stability of the Ti–WO_3 nanosheets (Fig. S7†).

To unravel the true active sites during CO_2 photoreduction over the Ti–WO_3 nanosheets, quasi *in situ* XPS spectra were used to investigate the change in electron density on the W sites. As shown in Fig. 4A and B, the content of W^{5+} increased distinctly upon light irradiation of the reaction system, indicating that the W sites accepted the photoexcited electrons and generated W^{5+} active species during the reaction. Once CO_2 was introduced into the system, the ratio of W^{5+}/W^{6+} decreased from 0.38 to 0.25, indicating that the W^{5+} ions were reoxidized into the original W^{6+} ions by donating electrons to the adsorbed CO_2 molecules.[43] In addition, the valence state of the W atoms recovered to the initial state after removing the light irradiation (Fig. 3C) and the same trend was also detected on the WO_3 nanosheets (Fig. S8†). Notably, the W^{5+} content in the Ti–WO_3 nanosheets was higher than that in the WO_3 nanosheets in the dark and it increased after the introduction of CO_2, implying that CO_2 was adsorbed on the W sites (Fig. 4D). On the contrary, the quasi *in situ* X-ray absorption near-edge spectroscopy (XANES) spectra revealed that the L-edge of Ti did not have any distinct changes during the whole process (Fig. S9†), indicating that the doped Ti atoms did not participate in the CO_2 photoreduction directly. This further certified that the true active sites over the Ti–WO_3 nanosheets were the W sites rather the Ti sites. Interestingly, the ratio of W^{5+}/W^{6+} on the Ti–WO_3 nanosheets was lower than that on the WO_3 nanosheets under light irradiation, suggesting that more photoexcited electrons were donated to the adsorbed CO_2 molecules for photoreduction. In other words, the Ti dopants could facilitate the charge transfer on the Ti–WO_3 nanosheets to enhance the CO_2RR performance, where the separation of photogenerated carriers on the Ti–WO_3 nanosheets was also promoted, as revealed by the impedance test, transient photocurrent response, photo-luminescence (PL) and time-resolved photoluminescence (TRPL) spectra (Fig. S10 and S11†).[17,31]

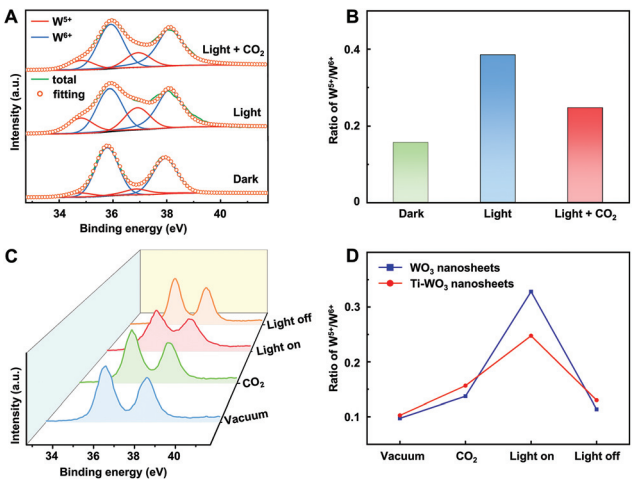

Fig. 4 (A) Quasi *in situ* XPS spectra and (B) the corresponding W^{5+}/W^{6+} ratio of the Ti–WO_3 nanosheets under different atmospheres. (C) Quasi *in situ* XPS spectra of the Ti–WO_3 nanosheets during the CO_2 photoreduction. (D) The comparison of the W^{5+}/W^{6+} ratio of the Ti–WO_3 nanosheets and the WO_3 nanosheets during the CO_2 photoreduction.

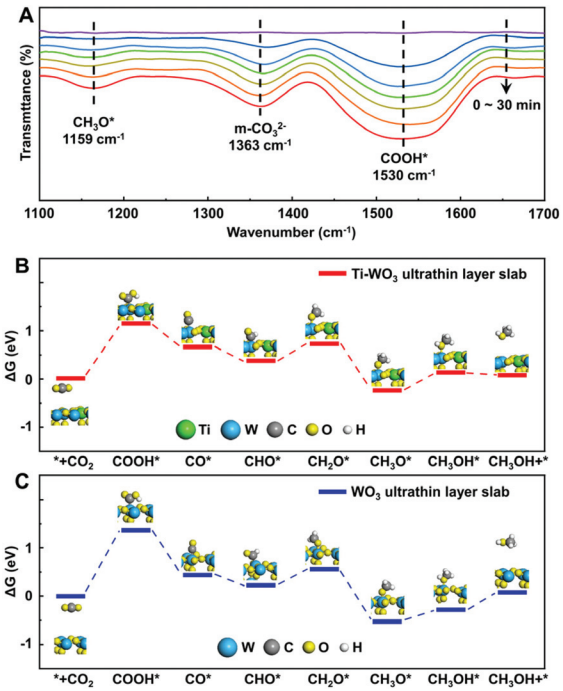

Fig. 5 (A) *In situ* FTIR spectra of the Ti–WO_3 nanosheets. (B) Free energy diagrams of CO_2 photoreduction to CH_3OH over the Ti–WO_3 ultrathin layer slab. (C) Free energy diagrams of CO_2 photoreduction to CH_3OH over the WO_3 ultrathin layer slab.

To find out the reaction intermediates of CH_3OH formation on the Ti–WO_3 nanosheets, *in situ* FTIR measurement was carried out. As shown in Fig. 5A, three peaks appeared at 1158 cm^{-1}, 1365 cm^{-1} and 1530 cm^{-1}. Similar peaks also appeared in the *in situ* FTIR spectra of the pristine WO_3 nanosheets, indicating the same CO_2 reduction process (Fig. S12†). The peak at 1530 cm^{-1} could be assigned to COOH*, which was one of the most important intermediates for carbon products during CO_2 reduction.[36,42,44] Meanwhile, it was found that the peak density of COOH* on the Ti–WO_3 nanosheets was higher than that on the WO_3 nanosheets (Fig. S12†), implying that the Ti dopants might benefit CH_3OH formation through promoting the generation of COOH* intermediates. The peak at 1365 cm^{-1} was assigned to *m*-CO_3^{2-}, which could be due to the dissolved CO_2 in the water.[45] In addition, the peak at 1158 cm^{-1} could be ascribed to CH_3O*, which was one of the intermediates for CH_3OH formation.[42,44] Based on the results of *in situ* FTIR spectra, the possible reaction pathways could be summarized as follows:

$$* + CO_2 + e^- + H^+ \rightarrow COOH* \quad (1)$$

$$COOH* + e^- + H^+ \rightarrow CO* + H_2O \quad (2)$$

$$CO* + e^- + H^+ \rightarrow CHO* \quad (3)$$

$$CHO^* + e^- + H^+ \rightarrow CH_2O^* \quad (4)$$

$$CH_2O^* + e^- + H^+ \rightarrow CH_3O^* \quad (5)$$

$$CH_3O^* + e^- + H^+ \rightarrow CH_3OH + * \quad (6)$$

where the asterisks denote catalytically active sites in the reaction.

To further reveal the reason for the promotion of CH_3OH formation on the Ti–WO_3 nanosheets, the Gibbs free energy of these key reaction pathways was calculated using DFT calculation (Fig. 5B and C and Table S4†). The calculation results suggested that the rate-limiting step was the formation of COOH* intermediates for both the samples,[46,47] while the reaction energy from CO_2 to COOH* was decreased from 1.37 to 1.15 eV over the Ti–WO_3 ultrathin layer slab, indicating a lower activation barrier of CO_2 on the WO_3 nanosheets after Ti doping. This could be attributed to the strengthened bonding between COOH* intermediates and the catalyst (Fig. S13†),[44] which could stabilize and generate more COOH* intermediates during the CO_2 photoreduction, well consistent with the *in situ* FTIR results. Furthermore, the energy barrier of CH_3OH desorption over the Ti–WO_3 ultrathin layer slab was −0.06 eV, obviously lower than that of 0.36 eV over the WO_3 ultrathin layer slab, implying that the Ti dopants could also facilitate the CH_3OH desorption, which was an important process for CH_3OH formation. Thus, it was rational to conclude that doping Ti into WO_3 nanosheets could lower the reaction energy barrier, stabilize the COOH* intermediates and make CH_3OH easier to desorb, thus improving the CH_3OH yield during the CO_2 photoreduction.

Conclusions

In summary, the ultrathin Ti-doped WO_3 nanosheets were successfully fabricated as an efficient catalyst for selectively photoreducing CO_2 and H_2O into CH_3OH. XPS, XANES and element mappings showed the successful doping of Ti into the WO_3 nanosheets, while the PL and TRPL spectra demonstrated that the separation of photogenerated carriers on the Ti-doped WO_3 nanosheets were significantly promoted. Quasi *in situ* XPS spectra and quasi *in situ* XANES spectra firmly confirmed that the true active sites were the W sites rather the Ti sites, where the Ti dopants could facilitate the charge transfer, which was beneficial for the formation of COOH* species. *In situ* FTIR spectroscopy demonstrated this conclusion through the stronger intensity of COOH* species on the Ti-doped WO_3 nanosheets, while DFT calculations showed that Ti doping could strengthen the bonding between COOH* intermediates and the catalyst. In addition, the Gibbs free energy calculations also indicated that the activation barrier of CO_2 was decreased from 1.37 to 1.15 eV, while the energy barrier of CH_3OH desorption was decreased from 0.36 to −0.06 eV on the Ti–WO_3 nanosheets, thus promoting the formation of CH_3OH. In consequence, the Ti-doped WO_3 ultrathin nanosheets exhibited a superior CH_3OH selectivity of 88.9% and achieved a methanol evolution rate of 16.8 μmol g^{-1} h^{-1}, about 3.3 times higher than that on the WO_3 nanosheets. This work offers an effective approach to photoreduce CO_2 into CH_3OH and renders a deep insight to promote the performance of catalysts during the photoreduction reaction.

Author contributions

Y. Xie, Y. F. Sun, P. Q. Ling and J. C. Zhu conceived the idea and co-wrote the paper. P. Q. Ling and Z. Q. Wang carried out the sample synthesis, characterization and CO_2 photoreduction measurement. J. C. Zhu conducted DFT calculations. J. Hu and J. F. Zhu conducted the quasi *in situ* XPS and quasi *in situ* XANES measurement. W. S. Yan conducted the synchrotron–radiation XANES measurement. All the authors contributed to the overall scientific interpretation and edited the manuscript.

Conflicts of interest

There are no conflicts to declare.

Acknowledgements

This work was financially supported by the National Key R&D Program of China (2019YFA0210004), the National Natural Science Foundation of China (22125503, 21975242, U2032212, 21890754), the Strategic Priority Research Program of Chinese Academy of Sciences (XDB36000000), the Youth Innovation Promotion Association of CAS (CX2340007003), the Major Program of Development Foundation of Hefei Center for Physical Science and Technology (2020HSC-CIP003), the Users with Excellence Program of Hefei Science Center CAS (2020HSC-UE001) and the University Synergy Innovation Program of Anhui Province (GXXT-2020-001). Supercomputing USTC and National Supercomputing Center in Shenzhen are acknowledged for computational support.

References

1 N. Kornienko, J. Z. Zhang, K. K. Sakimoto, P. Yang and E. Reisner, *Nat. Nanotechnol.*, 2018, **13**, 890–899.
2 X. B. Li, Z. K. Xin, S. G. Xia, X. Y. Gao, C. H. Tung and L. Z. Wu, *Chem. Soc. Rev.*, 2020, **49**, 9028–9056.
3 X. Li, J. Yu, M. Jaroniec and X. Chen, *Chem. Rev.*, 2019, **119**, 3962–4179.
4 X. Chang, T. Wang, P. Yang, G. Zhang and J. Gong, *Adv. Mater.*, 2019, **31**, 1804710.
5 S. Navarro-Jaén, M. Virginie, J. Bonin, M. Robert, R. Wojcieszak and A. Y. Khodakov, *Nat. Rev. Chem.*, 2021, **5**, 564–579.
6 H. Zhao, J. Duan, Z. Zhang and W. Wang, *ChemCatChem*, 2021, **14**, 202101733.

7 X. Chang, T. Wang, Z. J. Zhao, P. Yang, J. Greeley, R. Mu, G. Zhang, Z. Gong, Z. Luo, J. Chen, Y. Cui, G. A. Ozin and J. Gong, *Angew. Chem., Int. Ed.*, 2018, **57**, 15415–15419.
8 Z. H. Li, H. Zeng, G. Zeng, C. Ru, G. Li, W. Yan, Z. Shi and S. Feng, *Angew. Chem., Int. Ed.*, 2021, **60**, 26577–26581.
9 A. Goeppert, M. Czaun, J. P. Jones, G. K. Surya Prakash and G. A. Olah, *Chem. Soc. Rev.*, 2014, **43**, 7995–8048.
10 C. H. Vo, C. Mondelli, H. Hamedi, J. Pérez-Ramírez, S. Farooq and I. A. Karimi, *ACS Sustainable Chem. Eng.*, 2021, **9**, 10591–10600.
11 B. Han, X. Ou, Z. Deng, Y. Song, C. Tian, H. Deng, Y. J. Xu and Z. Lin, *Angew. Chem., Int. Ed.*, 2018, **57**, 16811–16815.
12 H. L. Nguyen and A. Alzamly, *ACS Catal.*, 2021, **11**, 9809–9824.
13 W. Guo, S. Liu, X. Tan, R. Wu, X. Yan, C. Chen, Q. Zhu, L. Zheng, J. Ma, J. Zhang, Y. Huang, X. Sun and B. Han, *Angew. Chem., Int. Ed.*, 2021, **60**, 21979–21987.
14 Y. Wang, X. Liu, X. Han, R. Godin, J. Chen, W. Zhou, C. Jiang, J. F. Thompson, K. B. Mustafa, S. A. Shevlin, J. R. Durrant, Z. Guo and J. Tang, *Nat. Commun.*, 2020, **11**, 2531.
15 S. C. Shit, I. Shown, R. Paul, K. H. Chen, J. Mondal and L. C. Chen, *Nanoscale*, 2020, **12**, 23301–23332.
16 M. Wang, M. Shen, X. Jin, J. Tian, M. Li, Y. Zhou, L. Zhang, Y. Li and J. Shi, *ACS Catal.*, 2019, **9**, 4573–4581.
17 Y. He, H. Rao, K. Song, J. Li, Y. Yu, Y. Lou, C. Li, Y. Han, Z. Shi and S. Feng, *Adv. Funct. Mater.*, 2019, **29**, 1905153.
18 M. Zhou, S. Wang, P. Yang, C. Huang and X. Wang, *ACS Catal.*, 2018, **8**, 4928–4936.
19 Y. Bo, C. Gao and Y. Xiong, *Nanoscale*, 2020, **12**, 12196–12209.
20 T. Kong, Y. Jiang and Y. Xiong, *Chem. Soc. Rev.*, 2020, **49**, 6579–6591.
21 Y. Mi, L. Wen, Z. Wang, D. Cao, R. Xu, Y. Fang, Y. Zhou and Y. Lei, *Nano Energy*, 2016, **30**, 109–117.
22 J. He, C. Wu, Y. Li and C. Li, *J. Mater. Chem. A*, 2021, **9**, 19508–19533.
23 F. Zhang, J. Zhang, B. Zhang, L. Zheng, X. Cheng, Q. Wan, B. Han and J. Zhang, *Nat. Commun.*, 2020, **11**, 1431.
24 Y. Zhao, Y. Zhao, G. I. N. Waterhouse, L. Zheng, X. Cao, F. Teng, L. Z. Wu, C. H. Tung, D. O'Hare and T. Zhang, *Adv. Mater.*, 2017, **29**, 1703828.
25 S. Qamar, F. Lei, L. Liang, S. Gao, K. Liu, Y. Sun, W. Ni and Y. Xie, *Nano Energy*, 2016, **26**, 692–698.
26 X. Li, L. Liang, Y. Sun, J. Xu, X. Jiao, X. Xu, H. Ju, Y. Pan, J. Zhu and Y. Xie, *J. Am. Chem. Soc.*, 2019, **141**, 423–430.
27 J. Fu, K. Liu, K. Jiang, H. Li, P. An, W. Li, N. Zhang, H. Li, X. Xu, H. Zhou, D. Tang, X. Wang, X. Qiu and M. Liu, *Adv. Sci.*, 2019, **6**, 1900796.
28 X. Li, S. Wang, L. Li, X. Zu, Y. Sun and Y. Xie, *Acc. Chem. Res.*, 2020, **53**, 2964–2974.
29 Y. Xu, J. Mo, G. Xie, X. Wang and S. Ding, *J. Mater. Chem. A*, 2020, **8**, 4457–4463.
30 T. Chen, T. Liu, X. Shen, W. Zhang, T. Ding, L. Wang, X. Liu, L. Cao, W. Zhu, Y. Li and T. Yao, *Sci. China Mater.*, 2021, **64**, 2997–3006.
31 L. K. Putri, B.-J. Ng, W.-J. Ong, H. W. Lee, W. S. Chang and S.-P. Chai, *J. Mater. Chem. A*, 2018, **6**, 3181–3194.
32 Y. Ding and P. Nagpal, *Nanoscale*, 2016, **8**, 17496–17505.
33 C. Mao, F. Zuo, Y. Hou, X. Bu and P. Feng, *Angew. Chem., Int. Ed.*, 2014, **53**, 10485–10489.
34 V. Kumaravel, J. Bartlett and S. C. Pillai, *ACS Energy Lett.*, 2020, **5**, 486–519.
35 S. Sun, M. Watanabe, J. Wu, Q. An and T. Ishihara, *J. Am. Chem. Soc.*, 2018, **140**, 6474–6482.
36 L. Liang, X. Li, Y. Sun, Y. Tan, X. Jiao, H. Ju, Z. Qi, J. Zhu and Y. Xie, *Joule*, 2018, **2**, 1004–1016.
37 J. Ma, K. Mao, J. Low, Z. Wang, D. Xi, W. Zhang, H. Ju, Z. Qi, R. Long, X. Wu, L. Song and Y. Xiong, *Angew. Chem., Int. Ed.*, 2021, **60**, 9357–9361.
38 B. M. Klepser and B. M. Bartlett, *J. Am. Chem. Soc.*, 2014, **136**, 1694–1697.
39 G. Cai, X. Wang, D. Zhou, J. Zhang, Q. Xiong, C. Gu and J. Tu, *RSC Adv.*, 2013, **3**, 6896–6905.
40 S. S. Kalanur, I.-H. Yoo and H. Seo, *Electrochim. Acta*, 2017, **254**, 348–357.
41 Y. Zhan, M. R. J. Tan, X. Cheng, W. M. A. Tan, G. F. Cai, J. W. Chen, V. Kumar, S. Magdassi and P. S. Lee, *J. Mater. Chem. C*, 2017, **5**, 9995–10000.
42 W. Shao, S. Wang, J. Zhu, X. Li, X. Jiao, Y. Pan, Y. Sun and Y. Xie, *Nano Res.*, 2021, **14**, 4520–4527.
43 S. Zhu, X. Li, X. Jiao, W. Shao, L. Li, X. Zu, J. Hu, J. Zhu, W. Yan, C. Wang, Y. Sun and Y. Xie, *Nano Lett.*, 2021, **21**, 2324–2331.
44 X. Li, Y. Sun, J. Xu, Y. Shao, J. Wu, X. Xu, Y. Pan, H. Ju, J. Zhu and Y. Xie, *Nat. Energy*, 2019, **4**, 690–699.
45 Y. Wang, J. Zhao, T. Wang, Y. Li, X. Li, J. Yin and C. Wang, *J. Catal.*, 2016, **337**, 293–302.
46 Y. Li, S. Wang, X. S. Wang, Y. He, Q. Wang, Y. Li, M. Li, G. Yang, J. Yi, H. Lin, D. Huang, L. Li, H. Chen and J. Ye, *J. Am. Chem. Soc.*, 2020, **142**, 19259–19267.
47 P. Yang, H. Zhuzhang, R. Wang, W. Lin and X. Wang, *Angew. Chem., Int. Ed.*, 2019, **58**, 1134–1137.